CHEMISTRY OF MATERIALS
Cite This: Chem. Mater. 2017, 29, 10027−10036
Article
pubs.acs.org/cm

Discovery and Characterization of a Pourbaix-Stable, 1.8 eV Direct Gap Bismuth Manganate Photoanode

Paul F. Newhouse,[†] Sebastian E. Reyes-Lillo,[‡,⊥,#] Guo Li,[‡,⊥,#] Lan Zhou,[†] Aniketa Shinde,[†] Dan Guevarra,[†] Santosh K. Suram,[†] Edwin Soedarmadji,[†] Matthias H. Richter,[†,◆] Xiaohui Qu,[§,∥] Kristin Persson,[‡,§,∥] Jeffrey B. Neaton,*[,‡,⊥,#,▽] and John M. Gregoire*[,†]

[†]Joint Center for Artificial Photosynthesis and [◆]Division of Chemistry and Chemical Engineering, California Institute of Technology, Pasadena, California 91125, United States

[‡]Joint Center for Artificial Photosynthesis, [§]Energy Technologies Area, and [⊥]Molecular Foundry, Lawrence Berkeley National Laboratory, Berkeley, California 94720, United States

[∥]Department of Materials Science and Engineering and [#]Department of Physics, University of California, Berkeley, California 94720, United States

[▽]Kavli Energy NanoSciences Institute, Berkeley, California 94720, United States

Supporting Information

ABSTRACT: Solar-driven oxygen evolution is a critical technology for renewably synthesizing hydrogen- and carbon-containing fuels in solar fuel generators. New photoanode materials are needed to meet efficiency and stability requirements, motivating materials explorations for semiconductors with (i) band-gap energy in the visible spectrum and (ii) stable operation in aqueous electrolyte at the electrochemical potential needed to evolve oxygen from water. Motivated by the oxygen evolution competency of many Mn-based oxides, the existence of several Bi-containing ternary oxide photoanode materials, and the variety of known oxide materials combining these elements with Sm, we explore the Bi−Mn−Sm oxide system for new photoanodes. Through the use of a ferri/ferrocyanide redox couple in high-throughput screening, $BiMn_2O_5$ and its alloy with Sm are identified as photoanode materials with a near-ideal optical band gap of 1.8 eV. Using density functional theory-based calculations of the mullite $Bi^{3+}Mn^{3+}Mn^{4+}O_5$ phase, we identify electronic analogues to the well-known $BiVO_4$ photoanode and demonstrate excellent Pourbaix stability above the oxygen evolution Nernstian potential from pH 4.5 to 15. Our suite of experimental and computational characterization indicates that $BiMn_2O_5$ is a complex oxide with the necessary optical and chemical properties to be an efficient, stable solar fuel photoanode.

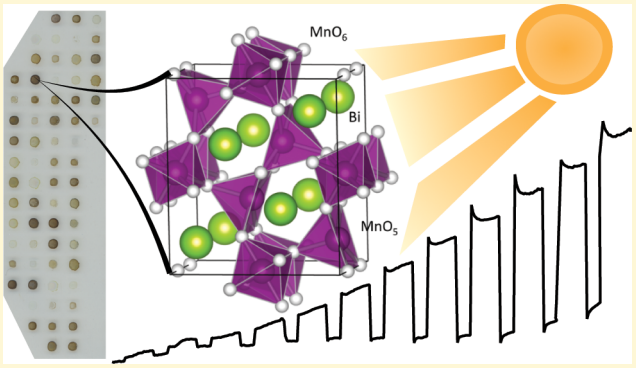

INTRODUCTION

To photoelectrochemically synthesize fuel, solar fuel generators couple the oxygen evolution reaction (OER) to a fuel-forming reaction, typically hydrogen evolution or carbon dioxide reduction.[1] Solar fuel generation comprises a promising renewable energy technology and is particularly desirable among renewable energy technologies due to the high-energy-density storage and transportation of chemical fuels. While efficient solar fuel generators can be created by use of tandem photoelectrochemical (PEC) cells, which combine an OER photoanode and a fuel-forming photocathode, widespread deployment of this technology is impeded by several technological challenges, most notably the development of an efficient and stable photoanode.[2−6]

While substantial technology development has proceeded through utilization of highly stable metal oxide photoanodes such as TiO_2 and WO_3, the optical absorption of these semiconductors is limited to the ultraviolet spectrum, substantially limiting solar conversion efficiency. Substantial effort has also been placed in the development of α-Fe_2O_3, which is remarkable for its combination of high stability under OER photoanode operating conditions and relatively low band-gap energy near 2 eV.[7,8] While the performance of α-Fe_2O_3 is limited by intrinsic charge-transport properties, it remains a fixture in solar fuel research because, until the present work, no other material has been shown to rival its stability and desirable band-gap energy. By combining high-throughput experimentation and materials theory, we identify $BiMn_2O_5$ as a photoanode that meets these stringent requirements. With Pourbaix stability over a broad pH range, it is a promising photoanode for device architectures that

Received: August 25, 2017
Revised: November 13, 2017
Published: November 13, 2017

DOI: 10.1021/acs.chemmater.7b03591
Chem. Mater. 2017, 29, 10027−10036

operate in near-neutral to strong-alkaline electrolytes. With a 1.8 eV direct band gap, its theoretical solar to fuel conversion efficiency in a tandem absorber system is in excess of 20%. According to the state-of-the-art device efficiency model, which includes several practical consequences of using earth-abundant materials, this 1.8 eV band gap is nearly optimal and can yield 15% solar to hydrogen conversion efficiency.[9]

In the compendium of metal oxide semiconductors being explored for solar fuel applications,[10] Bi-based ternary oxides play a prominent role, with $BiVO_4$ being the preeminent ternary metal oxide photoanode.[11] Other Bi-based phases include $BiFeO_3$[12] and $CuBi_2O_4$, the latter being a notable high-throughput discovery[13] that continues to show promise as an H_2-producing photocathode.[14] As highlighted by the recent demonstration of Bi_2MoO_6 as a photoanode,[15] overall water splitting with $Bi_2Ga_4O_9$-based materials,[16] and our recent high-throughput discovery campaigns based on ternary metal vanadates[17] and manganates,[18,19] photoactive ternary metal oxides are being discovered at an appreciable rate. There has also been a recent emergence in the experimental[20,21] and computational[22] investigation of quaternary oxide phases, wherein the utilization of three cation elements creates opportunities for detailed tuning of multifunctional properties.

For OER photoanodes, high-valent Mn cations are desirable components of an oxide semiconductor due to the native catalytic activity of these species[23] and the Pourbaix stability of $Mn^{4+}O_2$ near 1.23 V versus RHE (reversible hydrogen electrode).[24] While surface protection layers have garnered substantial interest in photoanode research,[25,26] decreasing the thermodynamic instability of the semiconductor remains crucial for (i) loosening requirements on the conformality of coating layers; (ii) enabling application of coating layers to boost performance through, for example, increasing catalytic activity and lowering surface recombination;[27,28] and (iii) establishing semiconductor−liquid junctions that accelerate charge separation within the semiconductor through band bending.

High-throughput methods have recently been developed for discovering[17,29−31] and optimizing[28,32−34] solar fuel photoanodes, and in the present work the discovery of $BiMn_2O_5$ as a photoanode was enabled through a combination of high-throughput synthesis, screening, and characterization. The ensuing theory-based assessment of its electronic structure advances our understanding of this material, not only for the present applications but also with respect to its multiferroic properties, which comprise the majority of the literature on this material.[35−39] Our collective results place bismuth manganate as a unique material among candidate photoanodes due to its combination of band gap and stability of α-Fe_2O_3 with key aspects of the $BiVO_4$ band character, motivating continued research to capitalize on its promise for enabling efficient solar fuel generation.

EXPERIMENTAL AND COMPUTATIONAL METHODS

Inkjet Printing. Discrete composition (Bi−Mn−Sm)-O_x pseudo-ternary libraries with 10 at. % step spacing were prepared via inkjet printing of 0.25 M aqueous-based solutions of $Bi(NO_3)_3{\cdot}5H_2O$ (Sigma, 98%), $Mn(NO_3)_2{\cdot}4H_2O$ (Alfa, 99.98%), and $Sm(NO_3)_3{\cdot}6H_2O$ (Sigma, 99.9%) onto Tec-15 FTO substrates with a Microfab Technologies JetLab4 inkjet printer. The Bi solution was prepared by first dissolving $Bi(NO_3)_3$ in 10 vol % HNO_3 with hot-plate stirring (50 °C) and then adjusting the salt concentration with diethylene glycol (DEG, Sigma, 99%) such that the final solution contained ∼7 vol % DEG at the above molarity. The Mn and Sm solutions were prepared from a 10 vol % solution of DEG in Millipore 18 MΩ water. Each printed sample was formed from 100 drops, corresponding to ∼1 nmol of metal ions in the ∼1-mm-diameter sample area. The metal precursors were converted to metal oxides via calcination in air at 615 °C for 1 h in a Thermo Scientific box oven (2 h ramp up, 1 h ramp down), although the oxygen stoichiometry was not characterized. An Epson V600 photoscanner was used to acquire 1200 dots per inch (dpi) images of each library following calcination.

Physical Vapor Deposition Synthesis. The Bi−Mn oxide composition library was fabricated by reactive direct current (dc) magnetron cosputtering of Bi and Mn metal targets onto 100-mm-diameter, 2.2-mm-thick glass substrates with a fluorine-doped tin oxide (FTO) coating (Tec7) in a sputter deposition system (Kurt J. Lesker Co., PVD75) with 10^{-5} Pa base pressure. It was deposited as a metal thin film under 0.80 Pa Ar working pressure. Composition gradients in the cosputtered continuous composition spreads were attained by positioning the deposition sources in a nonconfocal geometry. The deposition proceeded for 10 min with power on the Bi and Mn sources at 33 and 150 W, respectively. The as-deposited composition library was subsequently placed flat on a quartz support and annealed in a Thermo Scientific box oven in flowing air at 610 °C for 1 h. The annealing was preceded by a 2 h temperature ramp and was followed by natural cooling.

X-ray Diffraction. The crystal structure and phase distribution of the physical vapor deposition (PVD) composition library were determined through X-ray diffraction (XRD) measurements on a Bruker Discover D8 diffractometer with Cu Kα radiation from a Bruker IμS source. The X-ray spot size was limited to a 1 mm length scale, over which the composition is constant to within approximately 1%. The XRD measurements were performed on a series of evenly spaced positions along the composition gradient. Diffraction images were collected with a two-dimensional (2D) VÅNTEC-500 detector and integrated into one-dimensional (1D) patterns by use of DIFFRAC.-SUITE EVA software.

For inkjet composition libraries, XRD data were acquired via a custom HiTp setup incorporated into the bending-magnet beamline 1-5 of the Stanford Synchrotron Radiation Light Source (SSRL) at SLAC National Accelerator Laboratory. A detailed description of the experiment was provided by Gregoire et al.[40] Characterization of the (Bi−Mn−Sm)O_x library employed a monochromated 12.7 keV source in reflection scattering geometry with a 2D image detector (Princeton Quad-RO 430 4320). Diffraction images were processed into 1D XRD patterns (intensity vs scattering vector magnitude) by use of WxDiff software[41] and further processed with a custom background subtraction algorithm using cubic splines. Phase identification proceeded by identifying candidates in the International Crystallography Diffraction Database (ICDD) that best match the integrated 1D XRD patterns.

X-ray Fluorescence. X-ray fluorescence spectroscopy (EDAX Orbis Micro-XRF) was employed to measure select compositions of vapor-deposited and inkjet-prepared Bi−Mn oxide libraries with measurement spot size approximately 2 mm in diameter. Since the XRF sampling depth far exceeds the film thickness, thin-film standards for Mn and Bi (MicromatterTM) were used to calculate the molar loading (moles per substrate area) of these elements, which were divided to obtain Mn:Bi ratios. The Sm composition was not quantified, as a thin-film XRF standard was not available. For the sputter-deposited film with phase-pure $BiMn_2O_5$, bulk density was used to calculate the nominal film thickness from the XRF measurement.

UV−Visible Spectroscopy. Optical spectroscopy was performed by use of a custom dual-integrating sphere spectrometer described in detail previously.[51] Briefly, the fractional transmittance (T) and total reflection (R) were collected simultaneously as fiber illumination from a 200 W HgXe lamp was rastered over the sample surface. These signals were used to calculate the spectral absorption coefficient (α):

$$-\alpha\tau = \ln[T(1 - R)^{-1}]$$

where τ is the film thickness.

Photoectrochemistry Details. All (photo)electrochemistry experiments were performed in our previously published scanning droplet cell instrumentation, utilizing a potentiostat (Gamry G 300), custom automation software, and three-electrode cell.[52] For ferri/ferrocyanide

DOI: 10.1021/acs.chemmater.7b03591
Chem. Mater. 2017, 29, 10027−10036

(FCN) PEC measurements, the $[Fe(CN)_6]^{3-/4-}$ redox couple was added to 0.1 M NaOH electrolyte by dissolving 50 mM each potassium ferricyanide and potassium ferrocyanide, which was bubbled with N_2. The back contact of the samples was shorted to a Pt counter electrode, and the short-circuit current was measured with the solution poised at the redox couple potential of 0.36 V versus normal hydrogen electrode (NHE), which is approximately 0.1 V below the oxygen evolution potential in the 0.1 M NaOH electrolyte. Measurements in the absence of the FCN redox couple were performed in 0.1 M NaOH and 0.25 M sodium sulfate electrolyte bubbled with O_2 with a bias of 1.23 V versus RHE, which was applied via a Ag/AgCl reference electrode. Both the FCN-containing and FCN-free experiments were performed with toggled back-side illumination from ThorLabs M385F1 or M455F1 light-emitting diodes (LEDs; see Table S3)

Photoactivity in the presence of a sulfite hole acceptor was assessed by use of 0.1 M NaOH electrolyte with 0.25 M sodium sulfate and 0.01 M sodium sulfite in a three-electrode cell (Pt counter electrode and Ag/AgCl reference electrode) with front-side illumination. Toggled illumination was obtained via Doric LEDC4-385/Y/G/A_SMA with 387, 451, 515, and 603 nm LEDs (see Table S3). External quantum efficiency values were estimated from 60 s chronoamperometric measurements (Figure S2) with an illuminated area of 0.58 mm^2.

X-ray Photoelectron Spectroscopy. The sputter-deposited film was characterized in a Kratos Axis Nova system with a base pressure better than 3×10^{-9} Torr. A monochromatic Al Kα ($h\nu$ = 1486.69 eV) source with a power of 150 W was used for all measurements. Core-level spectra were taken with a pass energy of 10 eV and a step size of 25 meV. X-ray photoelectron spectroscopic (XPS) data were analyzed with CasaXPS.

Pourbaix Calculations. To assess the Pourbaix stability of $Bi_{0.33}Mn_{0.67}$, we employed the Materials Project Pourbaix Application (MP Pourbaix App),[42] a framework based on thermodynamic first principles and experimental data for solids and aqueous ions, respectively, with solution concentrations of 10^{-6} M for both Bi and Mn ions.

Electronic Structure Calculations. We performed spin-polarized density functional theory (DFT) calculations using the Heyd–Scuseria–Ernzerhof (HSE) hybrid functional,[43] where 25% of the generalized gradient approximation[44] exchange was replaced with exact Hartree–Fock exchange, and the long-range interaction was screened with a range separation parameter of 0.2 $Å^{-1}$. The HSE hybrid functional has been shown to systematically (if somewhat fortuitously) predict optical properties of weakly correlated systems in better agreement with experiments than traditional semilocal functionals.[45] Our HSE calculations used a plane-wave energy cutoff of 400 eV, a 4 × 4 × 4 Monkhorst–Pack[46] *k*-point grid, and projected augmented wave pseudopotentials with 5, 13, and 6 valence electrons for Bi, Mn, and O, respectively, from the Vienna ab initio simulation package (VASP) library.[47] Structural relaxations were performed with HSE until Hellmann–Feynman forces were smaller than 0.05 eV·$Å^{-1}$. Macroscopic polarization was computed with the HSE functional using the modern theory of polarization,[48] as implemented in VASP.

Band alignment of water redox potentials with respect to vacuum were computed with slab calculations. Due to the computational expense of calculations with the HSE functional, we used the revised generalized gradient approximation of Perdew, Burke, and Ernzerhof[44] plus Hubbard U method[49] (PBEsol+U) for our slab calculations. We found that different values of *U* lead to qualitatively similar results and we therefore reported results for the standard value *U* = 3.9 eV.[50] In this case, we used an energy cutoff of 400 eV and a tolerance threshold for atomic forces of 0.5 eV·$Å^{-1}$. Table S1 reported the most stable surfaces among several different slab orientations and terminations.[51,52]

RESULTS AND DISCUSSION

High-Throughput Photoanode Discovery by Inkjet Printing. The Bi–Mn–Sm oxide library shown in Figure 1a contains an array of 66 inkjet-printed samples comprising all possible mixtures of the three elements with 10% intervals. We have shown previously that while this synthesis method does not typically yield compact thin films that conformally coat the substrate, the sample quality is sufficient to enable mapping of optical and (photo)electrochemical properties.[53] Figure 1b is the result of an automated image reconstruction routine that crops a 1 mm^2 image of each sample from Figure 1a and arranges them according to their composition in a standard ternary composition diagram with the element orientation provided in Figure 1c.

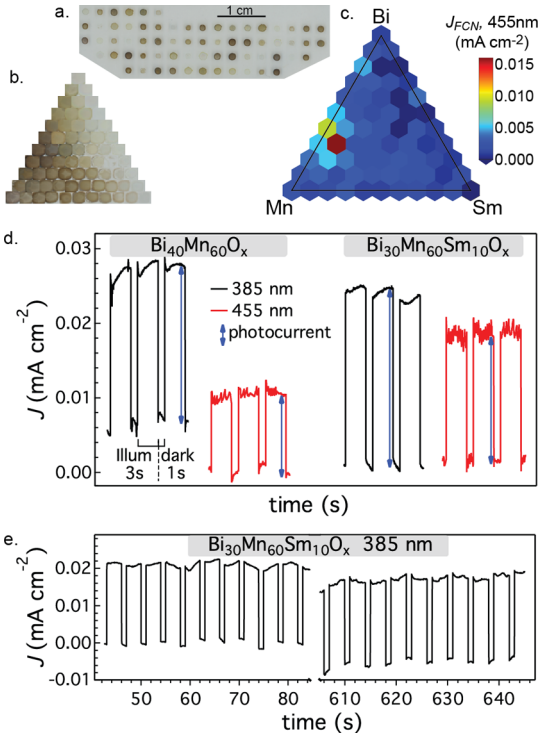

Figure 1. (a) Image of 66 inkjet-printed composition samples covering the Bi–Mn–Sm oxide space with 10% intervals. (b) Reconstruction of the randomized sample order into composition space. The orientation of the composition diagram is the same as panel c. (c) Short-circuit photocurrent density (J_{FCN}) after 40 s with 455 nm (158.7 mW·cm^{-2}) toggled illumination in pH 13 electrolyte poised by a ferri/ferrocyanide redox couple. (d) Toggled-illumination chronoamperometric data for the two top-performing samples with both 385 and 455 nm illumination (145.4 and 158.7 mW·cm^{-2}, respectively). (e) Portions of an extended (>10 min) measurement with 385 nm illumination for the $Bi_{30}Mn_{60}Sm_{10}O_x$ sample.

To identify photoactive oxides, we performed serial chopped-illumination chronoamperometry in the pH 13 electrolyte with FCN redox couple to poise the electrolyte potential approximately 0.1 V below the OER Nernstian potential.[53,54] The presence of anodic photocurrent in this condition indicates that the photoanode approximately meets the thermodynamic requirement for photoelectrocatalysis of the OER due to the similarity of the FCN redox potential and OER Nernstian potential. Since oxidation of the ferrocyanide to ferricyanide is a facile one-electron reaction, the thin-film photoactivity is measured without the substantial kinetic limitations for catalyzing the OER, which is a particular concern for high-throughput discovery of new oxide photoanodes because they are typically not synthesized with catalytic overlayers. Figure 1c shows the Bi–Mn–Sm composition map of the short-circuit photocurrent (J_{FCN}) after 40 s of toggled illumination with a 455 nm LED, revealing a photoactive region that extends from the Bi–Mn pseudobinary line into the pseudoternary composition space.

DOI: 10.1021/acs.chemmater.7b03591
Chem. Mater. 2017, 29, 10027–10036

For these samples, Figure 1d shows chronoamperometric traces for three illumination cycles with both 385 and 455 nm LEDs. Since small voltage fluctuations from the short-circuit condition can yield appreciable electrochemical current in the presence of the facile redox couple, the dark current in these measurements is typically not characteristic of the metal oxide sample, particularly if the dark current slowly fluctuates above and below zero, as is the case here (see Figure S1b).

Figure S1c shows photoactivity in the absence of the FCN redox couple for duplicates of the samples shown in Figure 1d. Compared to the FCN-containing measurements, these measurements were performed at a similar potential (1.23 V vs RHE) and in the same illumination configuration with approximately 20% higher irradiance. Without FCN, the quasi-steady-state photocurrent is approximately 10 times lower, and the current transients upon illumination toggling are much larger, indicating that kinetically limited charge transfer in the absence of the redox couple promotes increased charging and discharging of surface states.[55] These results highlight the importance of performing discovery experiments with a redox couple or sacrificial reagent and demonstrate that an optimized surface and/or overlayers are required to deploy these new materials as solar fuel photoanodes.

While thermodynamic stability modeling is presented below, we note here the evidence of stable photoactivity using the relatively short-duration materials discovery experiments: (i) The 385 nm chopping in the presence of FCN was extended to 650 s for the $Bi_{35}Mn_{60}Sm_{10}O_x$ sample and revealed no decay in photocurrent (Figure 1e). (ii) The photoanodic charge passed during this measurement is approximately 10^{-7} mol·cm^{-2} (moles of electrons or holes per thin film area), which is larger than the loading of Mn^{3+} in the film and indicates that the photoanodic current is not due to film oxidation. (iii) Film oxidation or corrosion is likely not altered by the presence or absence of the redox couple, so the much lower photocurrent in the absence of FCN (Figure S1c) demonstrates that photocorrosion does not comprise a substantial fraction of the photocurrent in the presence of the redox couple (Figure 1). (iv) The films did not visually appear to be altered by the PEC experiments. (v) This is further supported by post-PEC XRF measurements of the two samples in Figure 1d that reveal Mn:Bi ratios of 1.4 and 2.0, which are well within the 10% XRF uncertainty of the intended values of 1.5 and 1.9, respectively, for these samples; that is. the PEC experiments did not result in any preferential corrosion of Mn or Bi. A Sm peak was observed in the XRF measurement of the Sm-containing sample but was not quantified due to the lack of a thin-film Sm standard.

To identify the metal oxide phase(s) giving rise to this photoactivity, we turn to X-ray diffraction (XRD) characterization, which was acquired before PEC experiments on the samples used to generate Figure 1c. For brevity, we show in Figure 2 the XRD patterns for 12 compositions, the 11 along the Bi−Mn composition line and the $Bi_{30}Mn_{60}Sm_{10}O_x$ top performer from Figure 1c (see also Figure S3). Phase identification from the powder diffraction file database (ICDD PDF-4 + 2016) revealed that both $Bi_{40}Mn_{60}O_x$ and $Bi_{30}Mn_{60}Sm_{10}O_x$ samples appear to be, within the sensitivity of the measurement, phase-pure samples with the mullite $BiMn_2O_5$ crystal structure. Since both composition samples of interest in Figure 1 have the same phase, discovered as a photoanode through these experiments, we focus the remainder of the present work on further characterization and understanding of $BiMn_2O_5$ as a photoanode. That is, these results from inkjet-printed samples indicate

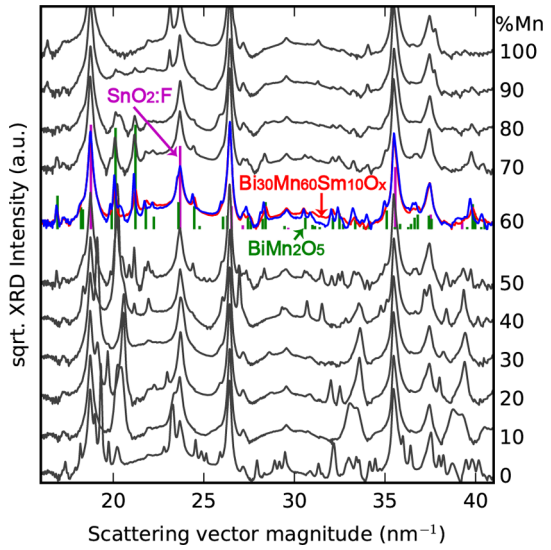

Figure 2. Synchrotron XRD patterns from 11 inkjet-printed Bi−Mn−O samples and $Bi_{30}Mn_{60}Sm_{10}O_x$, where each pattern contains substantial signal from the amorphous glass substrate and the SnO_2:F underlayer (magenta, ICDD 01-070-6153). The Bi−Mn and Bi−Mn−Sm samples with 60% Mn exhibit the highest phase purity of $BiMn_2O_5$ (green, 00-027-0048).

that Sm alloying on the Bi site increases photoanodic activity, and similar alloying of Sm^{3+} onto the Bi^{3+} site has recently been demonstrated to enhance charge separation in $BiVO_4$ photoanodes.[56] As discussed in that work, the large number of materials properties that change with alloying introduces challenges in determining the improvement mechanism, and since this mechanism cannot be understood without first understanding the base compound, we relegate further exploration of the Sm alloying to future work.

Photoelectrochemical and Optical Characterization of $BiMn_2O_5$. To provide additional photoelectrochemical characterization of $BiMn_2O_5$, a $Bi_{40}Mn_{60}O_x$ sample from a duplicate composition library was measured in a 0.1 M NaOH electrolyte with 0.25 M sodium sulfate and 0.01 M sodium sulfite, a hole acceptor with limited lifetime in the electrolyte that does not poise the solution potential in the same manner as the FCN redox couple but does alleviate the OER catalysis requirement for photoanodic current. Chopped-illumination chronoamperometry using LED wavelengths from 387 to 603 nm is shown in Figure S2, providing estimates of the spectral external quantum efficiency (EQE) under high-irradiance conditions (138−586 mW·cm^{-2}), as shown in the inset of Figure 3. The EQE results demonstrate photoactivity across most of the visible spectrum, and while Figure S2 shows higher photocurrent with 451 nm LED compared to 515 nm LED, the higher irradiance at 451 nm results in a lower EQE value, indicating that the EQE is irradiance-dependent and that more comprehensive monochromator experiments are required to map the spectral EQE at a specific irradiance. While the EQE values are all on the order of 0.1%, photoanodic current at 1.23 V versus RHE bias with photon energies below 2.1 eV is a rare feat in solar photochemistry and clearly demonstrates the opportunities $BiMn_2O_5$ provides for efficient solar utilization.

Figure 3 also shows a chopped-illumination cyclic voltammogram (CV) that starts at 1.2 V versus RHE and commences with a cathodic sweep that is followed by an anodic sweep to 1.36 V versus RHE. The CV reveals the presence of anodic photo-

DOI: 10.1021/acs.chemmater.7b03591
Chem. Mater. 2017, 29, 10027−10036

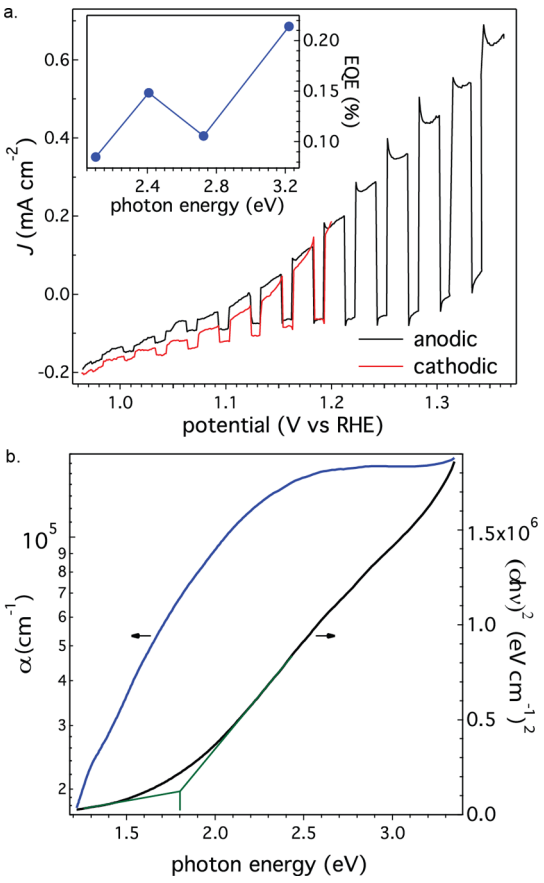

Figure 3. (a) Front-side toggled-illumination (385 nm, 413.1 mW·cm^{-2}) cyclic voltammogram of inkjet-printed $Bi_{40}Mn_{60}O_x$ starting with a cathodic sweep at 1.23 V vs RHE and finishing with an anodic sweep to 1.36 V vs RHE in pH 13 electrolyte with sodium sulfite hole acceptor. (Inset) Estimates of external quantum efficiency (EQE) in the same electrolyte for four different LEDs (λ = 387, 451, 515, and 603 nm; irradiance = 585.2, 378.7, 167.0, and 137.7 mW·cm^{-2}, respectively. (b) Optical analysis of a sputter-deposited $BiMn_2O_5$ thin film with determination of the 1.8 eV direct band gap illustrated with green lines.

current to the lower extent of the CV, which is 0.3 V below the OER Nernstian potential and was chosen as the low limit for these initial studies to avoid dark electrochemical reduction of Mn^{4+} (see below). The slowly varying dark current observed is larger than we typically observe for capacitive charging and also is not indicative of film redox reactions; fortunately, the photoactivity and its variation with potential are readily observed despite the dark current of unknown origin. The irradiance in this experiment is approximately 4 times larger than the FCN experiments of Figure 1 (both with approximately 385 nm LED, see Table S3), and the increase in photocurrent is even larger for this front-side-illuminated sulfite oxidation. While these results indicate that front-side illumination provides higher photoactivity for this inkjet-printed material, the exposed back contact in these porous materials induce a shunting current that lowers the FCN photocurrent but not the relatively irreversible sulfite oxidation, limiting direct comparison of the respective photocurrents.

In Figure S4, we present additional photoelectrochemical experiments that complement Figures 1−3, most importantly the resynthesis of $BiMn_2O_5$ using a more traditional technique, magnetron sputter codeposition, where the use of a continuous composition spread technique provides access to higher composition resolution than that of the discrete inkjet libraries. The XRD and photoelectrochemiscal experiments with this library provide more definitive demonstration that the maximum photocurrent in the Bi−Mn−O system is obtained with phase-pure $BiMn_2O_5$ (see Figure S4).

Since the sputtered thin film has a more uniform thickness than the inkjet-based material, a phase-pure $BiMn_2O_5$ sample from the sputter-deposited library was used for optical characterization. UV−vis spectroscopy, combined with the XRF-determined film thickness of 278 nm, provided the spectral absorbance (α) and Tauc spectrum for direct-allowed optical transitions, $(\alpha h\nu)^2$, as shown in Figure 3b. Per the Tauc formalism,[57] $BiMn_2O_5$ exhibits a direct-allowed (optical) band gap of approximately 1.8 eV with a subgap absorption tail, from which the presence or energy of a lower indirect-allowed transition could not be ascertained. Figure 3b also demonstrates that $BiMn_2O_5$ is highly absorbing in the visible range, with absorbance reaching 10^5 cm^{-1} at approximately 2 eV, motivating the study of thinner films in future work.

XPS characterization of the annealed, sputter-deposited $BiMn_2O_5$ sample is summarized in Figure 4. While XRF

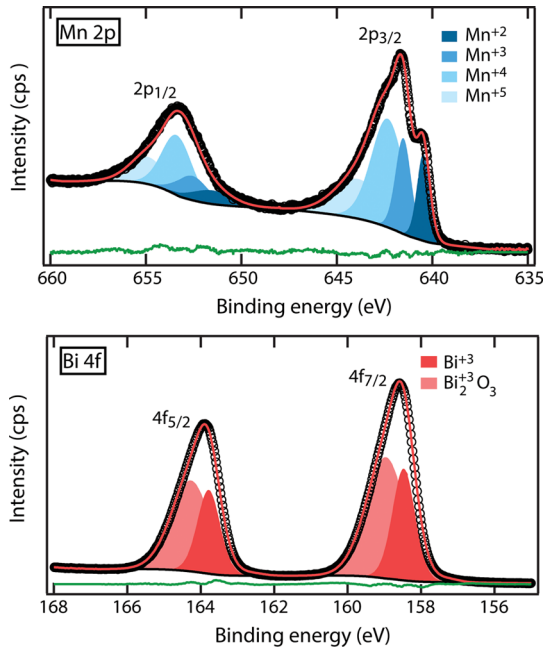

Figure 4. XPS characterization of sputter-deposited $BiMn_2O_5$ film after annealing. Black circles indicate the measured spectra, which are modeled with the background shown and component fitting that results in the envelope (red trace) and small residual signal (green). The four fitted Mn components match well to literature values for the labeled valences, and one Bi component matches that of pure Bi^{3+} oxide with the other appearing as the same valence with a small shift to lower binding energy.

measurements reveal that the bulk Mn:Bi is in excellent agreement with the formula unit stoichiometry (2.0 ± 0.2), the value obtained from XPS quantification of Mn 2p and Bi 4f peaks is approximately 1.5 ± 0.3, indicating a Bi-enriched surface. The Mn 2p spectrum is typically difficult to interpret, as demonstrated by precedence for fitting of Mn 2p from Mn_2O_3 using five components.[58] Valence-dependent binding energies for both Mn and Bi were recently summarized,[59] providing the labeling of the fitted components in Figure 4. While the fitting clearly shows the presence of the +3 and +4 valences of Mn as

DOI: 10.1021/acs.chemmater.7b03591
Chem. Mater. 2017, 29, 10027−10036

expected from the bulk structure, components at both higher and lower binding energy are also observed. The Bi 4f signal is well modeled by two components, with the higher binding energy one matching that of Bi_2O_3. We assert that the second component at slightly lower binding energy is also Bi^{3+} in a different chemical environment. Given the complexity of these signals and the disconnect between the vacuum and PEC environments, these measurements cannot directly identify the chemical nature of the operational surface and instead indicate substantial opportunity to better control surface chemistry, which may lead to enhanced PEC performance.

$BiMn_2O_5$ Stability and Pourbaix Diagram. The stable photoanodic response in Figure 1 provides important evidence that $BiMn_2O_5$ is a stable photoanode. The intrinsic operational stability of $BiMn_2O_5$ may be due to either thermodynamic stability under these (photo)electrochemical conditions or the formation of a self-passivation layer that does not (completely) inhibit photoanodic current, as recently explored for several copper vanadate photoanodes.[60] The calculated Bi−Mn Pourbaix diagram is shown in Figure 5, where the phase field

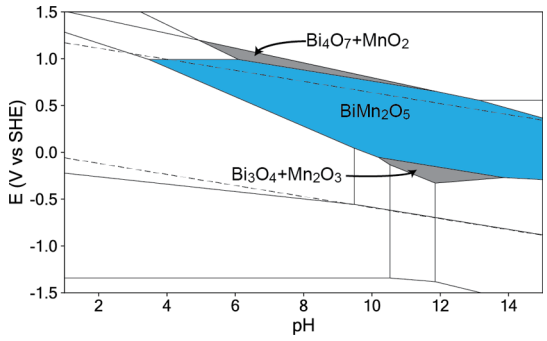

Figure 5. Calculated diagram of $Bi_{0.33}Mn_{0.67}$ at 10^{-6} mol·kg^{-1} Bi and Mn. The three phase fields with stable oxides are highlighted and labeled. Dashed lines correspond to 0 and 1.23 V vs RHE, where $BiMn_2O_5$ is the stable phase from pH 4.5 to 15.

in which $BiMn_2O_5$ is thermodynamically stable is highlighted, which at 1.23 V versus RHE spans pH 4.5−15, nearly the same range as Fe_2O_3 (see Figure S5). This pH range of stability at 1.23 V versus RHE is approximately the union (rather than the intersection) of the corresponding pH ranges for $Mn^{4+}O_2$ and $Bi_3^{3+}Bi^{5+}O_7$, demonstrating the importance of the mullite $BiMn_2O_5$ structure in stabilizing the Mn^{3+}, Mn^{4+} and Bi^{3+} cations (see Figure S6). Bolstered by the excellent visible response (Figure 3) and Pourbaix stability (Figure 5), we turn to computational characterization of the electronic structure to assess both the origins of these desirable properties of $BiMn_2O_5$ and opportunities for improving its performance as a photoanode.

Electronic Structure Characterization. To understand the interplay between structural, electronic, and magnetic degrees of freedom in $BiMn_2O_5$, we perform additional spin-polarized first-principles density functional theory (DFT) calculations using VASP[61] with the Heyd−Scuseria−Ernzerhof (HSE) hybrid functional.[43] As evidenced by prior work on the multiferroic properties of $BiMn_2O_5$,[35−39] the coupling between magnetic and electronic properties poses substantial challenges for electronic structure calculations, particularly due to the need to assign magnetic ordering. Experimental measurements have shown that $BiMn_2O_5$ is paramagnetic at room temperature and antiferromagnetic below its Neel temperature of 39 K.[35] Importantly, the low-temperature phase displays a small macroscopic polarization of 0.04 μC·cm^{-2}.[35] To account for the random orientation of the spins at room temperature, the temperature of relevance to the photoelectrochemical measurements, we infer attributes of paramagnetic $BiMn_2O_5$ by considering several spin configurations within a conventional eight formula unit supercell. We note that more accurate calculations of the electronic structure, and in particular the band-gap energy, would require simulation of the paramagnetic state and use of a higher level of theory such as ab initio many-body perturbation theory,[62] both of which carry substantial computational expense.

Our calculations focus on the room-temperature mullite structure of $BiMn_2O_5$, which is orthorhombic with the *Pbam* space group. The structure consists of an array of edge-sharing MnO_6 oxygen octahedra and corner-sharing MnO_5 square-pyramidal oxygen motifs, as shown in Figure 6. The Bi atoms are

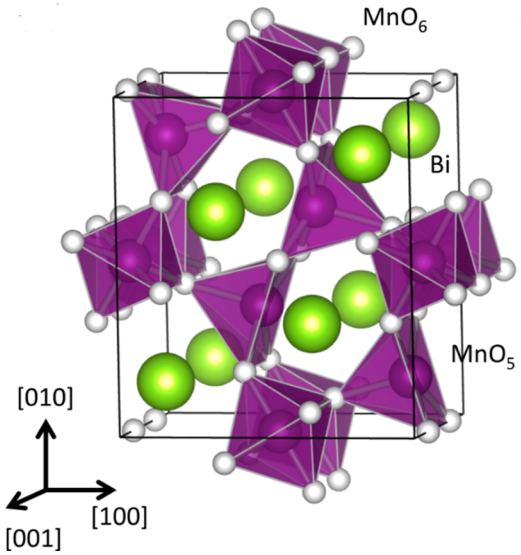

Figure 6. Crystal structure of $BiMn_2O_5$. Bi, Mn, and O atoms are shown as green, purple, and white spheres, respectively. MnO_6 octahedra and MnO_5 square-pyramids polyhedral are shown in violet.

surrounded by four octahedra and four square-pyramids, forming highly distorted BiO_8 oxygen cages. The magnetic configurations considered in the present work, which are illustrated nicely in ref 36, include ferromagnetic ordering (FM), two different antiferromagnetic orderings (AFM-1 and AFM-2), and ferrimagnetic ordering (FERRI). Total energy calculations using the HSE functional show that AFM-2 is the ground state among the magnetic configurations considered (see Table S1), which is in agreement with Zhang et al.[36] and commensurate with the type of ordering observed in related materials.[63,64] We find that the HSE lattice constants of the relaxed structures are within 1−2% of literature experimental values (see Table S1).[65] In addition, AFM-2 breaks inversion symmetry and displays a computed macroscopic polarization of 0.23 μC·cm^{-2} along the [010] axis. Since the Neel energy is on the order of 3 meV, we select AFM-2 as the most representative magnetic structure of the paramagnetic room-temperature phase,[66] and for the purposes of the present work we consider all four configurations.

Having elucidated the properties of the ground state, we compute the atom-projected density of states (PDOS) and plot the band structure for each magnetic configuration using HSE. The collection of band structures and PDOS are reported in

DOI: 10.1021/acs.chemmater.7b03591
Chem. Mater. 2017, 29, 10027−10036

Figures S7 and S8, and the results for the AFM-2 configuration are shown for convenience in Figure 7. While these data contain a wealth of information, we focus the present discussion on the properties most pertinent for their application as solar fuel photoanodes.

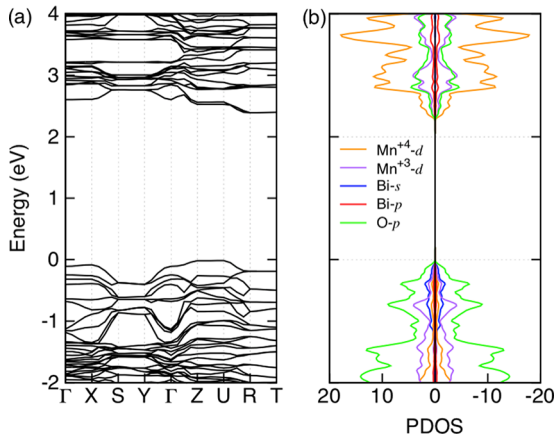

Figure 7. (a) Band structure and (b) projected density of states (PDOS) for the AFM-2 spin configuration using the HSE functional. The Fermi level corresponds to the highest occupied level. The symmetry points correspond to Γ = (0, 0, 0), X = (0.5, 0, 0), S = (0.5, 0.5, 0), Y = (0, 0.5, 0), Z = (0, 0, 0.5), U = (0.5, 0, 0.5), R = (0.5, 0.5, 0.5), and T = (0, 0.5, 0.5).

A summary of relevant parameters is provided in Table 1. The band gap is typically an indirect-allowed (IA) transition as shown in Figure 7a, with the direct-allowed (DA) gap at slightly higher energy, between 0.03 and 0.1 eV in the HSE band structure of Figure S7. This is consistent with the experimental observation of a direct-allowed band gap and classifies $BiMn_2O_5$ as a pseudo-direct-gap semiconductor. Among the magnetic configurations, we find that HSE band gaps are consistently higher than the 1.8 eV optical gap of Figure 3b by about 18%. For comparison, band gaps computed with the Hubbard U extension of the revised generalized gradient approximation (PBEsol+U)[44,49] underestimate band gaps by 58% with U = 3.9 eV (see Table 1). The discrepancies with experiment are expected for this level of theory and may be largely explained by strong on-site correlation effects associated with electrons in frontier Mn 3d orbitals.

While the band-gap energy varies somewhat with magnetic configuration, the much more sensitive aspect of the electronic structure is band dispersion. The FM and FERRI band diagrams of Figure S7 exhibit remarkably parabolic bands (see Table S4), indicating that FM and FERRI $BiMn_2O_5$ feature small electron and hole effective masses that promote facile band transport. In the AFM-1 and AFM-2 configurations, the bands become less disperse, suggesting reduced mobilities of electrons and holes. The latter results motivate future experimental efforts to determine the relationship between the effective masses in paramagnetic $BiMn_2O_5$ and the band structures with magnetic ordering. The elemental band character is relatively insensitive to magnetic configuration. As summarized in Table 1 and shown in Figure 6b and Figure S2, all spin configurations considered in this work exhibit substantial Bi^{3+} 6s character and Mn^{4+} 3d character at the valence band (VB) and conduction band (CB), respectively.

To delve deeper into band character, it is illustrative to compare and contrast with monoclinic $BiVO_4$,[11] which has received substantial attention as a solar fuel photoanode material due to its reasonable band-gap energy and carrier transport.[67,68] The $BiVO_4$ VB has Bi 6s and O 2p character similar to $BiMn_2O_5$, and its band dispersion is within the range of dispersions exhibited by the different magnetic configurations of $BiMn_2O_5$. The visible band gap of $BiVO_4$ is largely the result of low-lying unoccupied V^{5+} 3d states, for which the analogue in $BiMn_2O_5$ is the Mn^{4+} 3d states that are the majority species in nearly all the PDOS calculations, regardless of the choice of functional and the magnetic configuration. These unoccupied Mn^{4+} 3d states enable hybridization between the lone pair Bi 6s and O 2p states, and the corresponding benefits on the VB energy level are explored below. Overall, the striking similarities between the band character of $BiMn_2O_5$ and $BiVO_4$ indicate that the approaches for advancing the understanding and performance of $BiVO_4$ over the past decade may be leveraged for accelerated development of $BiMn_2O_5$.

Band-Edge Position Calculations. To study the band alignment of the system with respect to water redox potentials, we consider several surface terminations of $BiMn_2O_5$. The absolute position of the VB is obtained by first computing the bulk work function of the system with respect to vacuum using slab calculations, and then rigidly shifting the bulk edge state's Fermi level to that of the slab electronic calculation. Figure 8a,b shows the structure and potential energy for one of the lowest energy surface structure along the crystallographic ⟨111⟩ direction. For simplicity, we perform the calculations in the FM state.

The absolute position of the VB with respect to vacuum for the rest of the magnetic structures can be estimated by aligning the 1s oxygen core-level states at approximately 500 eV below the Fermi level. The energy difference between the VB of the FM and AFM-2 structures is approximately 0.3 eV, indicating that the VB alignment results of Figure 8 are not highly sensitive to magnetic ordering.

Table S2 shows the orientation, formation energy, and work function for the energy slab surfaces considered in this work, with the corresponding VB and CB energies shown in Figure 8c for slab calculations on the six surfaces with surface energy less than 80 meV per formula unit above hull. These results indicate that

Table 1. Band Gaps and Frontier Orbital Character for Magnetic Configurations of $BiMn_2O_5$ by Use of the HSE Functional[a]

	E_g (eV)			% Bi 6s in VB		% Mn 3d in CB	
magn config	HSE	PBEsol+U	DA − IA, HSE	PBEsol+U	HSE	PBEsol+U	HSE
AFM-2	2.44	1.12	0.10	14	18	55	61
FM	1.74	0.30	0.09	13	16	58	62
AFM-1	2.50	1.13	0.03	11	14	54	61
FERRI	2.29	0.97	0.10	16	19	57	60

[a]For comparison, we include band gaps and frontier orbital character computed with PBEsol+U with U = 3.9 eV. The characters are computed above CB and below VB within an energy window of 0.1 eV.

DOI: 10.1021/acs.chemmater.7b03591
Chem. Mater. 2017, 29, 10027−10036

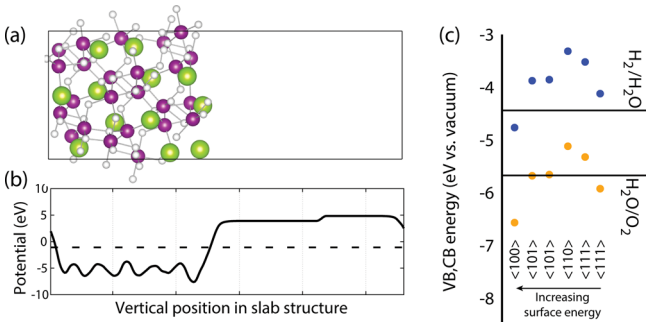

Figure 8. (a) $BiMn_2O_5$ ⟨111⟩ surface, which has the lowest surface energy among the structures considered in this work. Atoms are denoted as in Figure 6. A 1.5 nm vacuum layer is used for level-alignment calculations. (b) Potential energy along the vertical direction ⟨111⟩ of the slab structure, calculated using FM ordering. The Fermi level is denoted by the dashed line. (c) Band-level alignment for the six low-surface-energy surfaces of $BiMn_2O_5$ with different orientations and/or terminations. Each VB energy (orange) is determined from the calculated work function (see Table S2), and the CB energy (blue) is determined from the calculated work function using the experimental band gap of 1.8 eV, which is similar to the 1.74 eV HSE band gap. The rightmost result corresponds to the ⟨111⟩ lowest-energy surface in panel a, and the surface energies of the other five slabs are within 80 meV per formula unit.

the set of exposed facets at the front (liquid electrolyte) and back (metal) contacts are critical for understanding and controlling the semiconductor behavior. While four of the six low-energy surfaces exhibit work functions within a 0.6 eV range, the range of work function for the full set of six surfaces is in excess of 1.4 eV, indicating that the band alignment to water redox potentials and the attainable photovoltage are sensitive to crystallite orientation and termination.

Our XRD characterization of the PVD thin film indicates that the crystallites are randomly oriented such that the distribution of exposed facets is determined by the terminations of the powderlike grains (Figure S3). Consequently, we estimate the work function of bulk FM $BiMn_2O_5$ as the average of work functions of the six low-energy surfaces, which is 5.71 eV and places the VB energy approximately 0.34 eV below the OER equilibrium energy. Upon immersion in an aqueous electrolyte, a surface dipole may shift the VB potential further toward vacuum, and since dipole shifts up to 0.5 V have been observed for metal oxides, the operational VB potential of $BiMn_2O_5$ appears to be very well aligned with the OER Nernstian potential. We note that while slab calculations provide only an estimate of the operational band level alignment, these results are in agreement with experiment, as the well-aligned VB potential results in OER kinetic limitations, which explains the substantial increase in photocurrent upon addition of a facile redox couple or hole acceptor.

CONCLUSION

Driven by the discovery of a variety of metal oxide photoanodes over the past few years, recent efforts have taken multifaceted approaches to identify properties that may intrinsically limit the performance of emerging photoanode materials.[69,70] These one-material-at-a-time deep dives are motivated by the need to find materials that outperform the status quo α-Fe_2O_3 and $BiVO_4$ photoanodes. We identify $BiMn_2O_5$ as an excellent candidate for such studies, in part due to similarities between its conduction and valence band characters and those of $BiVO_4$ but most notably because its visible absorption and electrochemical stability are not surpassed by any known metal oxide photoanode. The indication that the valence band position lies near the OER Nernstian potential and the observation of increased photocurrent with Sm alloying suggest that the radiative efficiency of $BiMn_2O_5$ may be increased through optimization studies, ultimately providing efficient solar OER photoelectrocatalysis upon integration of an optimized catalyst.

ASSOCIATED CONTENT

Supporting Information

The Supporting Information is available free of charge on the ACS Publications website at DOI: 10.1021/acs.chemmater.7b03591.

Eight figures and four tables with raw photoelectrochemical data, combinatorial measurements on PVD library, additional Pourbaix diagrams, electronic structure and cell parameters for four computed magnetic configurations, and slab calculation details (PDF)

AUTHOR INFORMATION

Corresponding Authors

*E-mail jbneaton@lbl.gov (J.B.N.).
*E-mail gregoire@caltech.edu (J.M.G.).

ORCID

Santosh K. Suram: 0000-0001-8170-2685
John M. Gregoire: 0000-0002-2863-5265

Notes

The authors declare no competing financial interest.

ACKNOWLEDGMENTS

This material is based upon work performed by the Joint Center for Artificial Photosynthesis, a DOE Energy Innovation Hub, supported through the Office of Science of the U.S. Department of Energy (Award DE-SC0004993). Use of the Stanford Synchrotron Radiation Lightsource, SLAC National Accelerator Laboratory, is supported by the U.S. Department of Energy, Office of Science, Office of Basic Energy Sciences under Contract DE-AC02-76SF00515. Pourbaix diagram computation was supported by the Materials Project (BES DOE Grant EDCBEE). Work at the Molecular Foundry was supported by the Office of Science, Office of Basic Energy Sciences, of the U.S. Department of Energy under Contract DE-AC02-05CH11231. We thank Apurva Mehta, Fang Ren, Douglas G. Van Campen, Tim Dunn, and Ryan Jones for assistance with collection of synchrotron XRD data.

REFERENCES

(1) Pinaud, B. A.; Benck, J. D.; Seitz, L. C.; Forman, A. J.; Chen, Z.; Deutsch, T. G.; James, B. D.; Baum, K. N.; Baum, G. N.; Ardo, S.; Wang, H.; Miller, E.; Jaramillo, T. F. Technical and economic feasibility of centralized facilities for solar hydrogen production via photocatalysis and photoelectrochemistry. *Energy Environ. Sci.* **2013**, *6* (7), 1983–2002.

(2) Osterloh, F. E.; Parkinson, B. A. Recent developments in solar water-splitting photocatalysis. *MRS Bull.* **2011**, *36* (1), 17–22.

(3) Walter, M. G.; Warren, E. L.; McKone, J. R.; Boettcher, S. W.; Mi, Q.; Santori, E. A.; Lewis, N. S. Solar water splitting cells. *Chem. Rev.* **2010**, *110* (11), 6446–6473.

(4) Lewerenz, H.-J.; Peter, L. *Photoelectrochemical Water Splitting: Materials, Processes and Architectures*. The Royal Society of Chemistry: 2013; DOI: 10.1039/9781849737739.

DOI: 10.1021/acs.chemmater.7b03591
Chem. Mater. 2017, 29, 10027–10036

(5) Hu, S.; Xiang, C.; Haussener, S.; Berger, A. D.; Lewis, N. S. An analysis of the optimal band gaps of light absorbers in integrated tandem photoelectrochemical water-splitting systems. *Energy Environ. Sci.* **2013**, *6* (10), 2984.
(6) Haussener, S.; Xiang, C.; Spurgeon, J. M.; Ardo, S.; Lewis, N. S.; Weber, A. Z. Modeling, simulation, and design criteria for photoelectrochemical water-splitting systems. *Energy Environ. Sci.* **2012**, *5* (12), 9922−9935.
(7) Gilbert, B.; Frandsen, C.; Maxey, E. R.; Sherman, D. M. Band-gap measurements of bulk and nanoscale hematite by soft x-ray spectroscopy. *Phys. Rev. B* **2009**, *79* (3), 035108.
(8) Moniz, S. J. A.; Shevlin, S. A.; Martin, D. J.; Guo, Z.-X.; Tang, J. Visible-light driven heterojunction photocatalysts for water splitting − a critical review. *Energy Environ. Sci.* **2015**, *8*, 731−759.
(9) Fountaine, K. T.; Lewerenz, H. J.; Atwater, H. A. Efficiency limits for photoelectrochemical water-splitting. *Nat. Commun.* **2016**, *7*, 13706.
(10) Sivula, K.; van de Krol, R. Semiconducting materials for photoelectrochemical energy conversion. *Nature Reviews Materials* **2016**, *1*, 15010−15010.
(11) Sayama, K.; Nomura, A.; Zou, Z.; Abe, R.; Abe, Y.; Arakawa, H. Photoelectrochemical decomposition of water on nanocrystalline $BiVO_4$ film electrodes under visible light. *Chem. Commun.* **2003**, *23*, 2908−2909.
(12) Chen, X. Y.; Yu, T.; Gao, F.; Zhang, H. T.; Liu, L. F.; Wang, Y. M.; Li, Z. S.; Zou, Z. G.; Liu, J.-M. Application of weak ferromagnetic $BiFeO_3$ films as the photoelectrode material under visible-light irradiation. *Appl. Phys. Lett.* **2007**, *91* (2), No. 022114.
(13) Arai, T.; Konishi, Y.; Iwasaki, Y.; Sugihara, H.; Sayama, K. High-throughput screening using porous photoelectrode for the development of visible-light-responsive semiconductors. *J. Comb. Chem.* **2007**, *9* (4), 574−81.
(14) Berglund, S. P.; Abdi, F. F.; Bogdanoff, P.; Chemseddine, A.; Friedrich, D.; van de Krol, R. Comprehensive Evaluation of $CuBi_2O_4$ as a Photocathode Material for Photoelectrochemical Water Splitting. *Chem. Mater.* **2016**, *28* (12), 4231−4242.
(15) Tang, D.; Mabayoje, O.; Lai, Y.; Liu, Y.; Mullins, C. B. Enhanced Photoelectrochemical Performance of Porous Bi2MoO6 Photoanode by an Electrochemical Treatment. *J. Electrochem. Soc.* **2017**, *164* (6), H299−H306.
(16) Yang, J.; Jiang, P.; Yue, M.; Yang, D.; Cong, R.; Gao, W.; Yang, T. $Bi_2Ga_4O_9$: An undoped single-phase photocatalyst for overall water splitting under visible light. *J. Catal.* **2017**, *345*, 236−244.
(17) Yan, Q.; Yu, J.; Suram, S. K.; Zhou, L.; Shinde, A.; Newhouse, P. F.; Chen, W.; Li, G.; Persson, K. A.; Gregoire, J. M.; Neaton, J. B. Solar fuels photoanode materials discovery by integrating high-throughput theory and experiment. *Proc. Natl. Acad. Sci. U. S. A.* **2017**, *114* (12), 3040−3043.
(18) Shinde, A.; Suram, S. K.; Yan, Q.; Zhou, L.; Singh, A. K.; Yu, J.; Persson, K. A.; Neaton, J. B.; Gregoire, J. M. Discovery of Manganese-Based Solar Fuel Photoanodes via Integration of Electronic Structure Calculations, Pourbaix Stability Modeling, and High-Throughput Experiments. *ACS Energy Letters* **2017**, *2*, 2307−2312.
(19) The $BiMn_2O_5$ phase of the present work was not considered in this previously reported computational search because its 32 atoms per unit cell exceeds the threshold used in that work.
(20) Liu, H.; Nakamura, R.; Nakato, Y. A Visible-Light Responsive Photocatalyst, $BiZn_2VO_6$, for Efficient Oxygen Photoevolution from Aqueous Particulate Suspensions. *Electrochem. Solid-State Lett.* **2006**, *9* (5), G187−G190.
(21) Qiao, X.; Huang, Y.; Seo, H. J. Optical property and visible-light-driven photocatalytic activity of inverse spinel $LiNiVO_4$ nanoparticles prepared by Pechini method. *Appl. Surf. Sci.* **2014**, *321*, 488−494.
(22) Babaryk, A. A.; Odynets, I. V.; Khainakov, S.; Garcia-Granda, S.; Slobodyanik, N. S. Polyanionic identity of $Ca_2Zn_2(V_3O_{10})(VO_4)$ photocatalyst manifested by X-ray powder diffraction and periodic boundary density functional theory calculations. *CrystEngComm* **2015**, *17* (40), 7772−7777.
(23) Kurz, P. Biomimetic Water-Oxidation Catalysts: Manganese Oxides. In *Solar Energy for Fuels*; Tüysüz, H., Chan, C. K., Eds.; Topics in Current Chemistry, Vol. *371*; Springer International Publishing: 2016; pp 49−72; DOI: 10.1007/128_2015_634.
(24) Pourbaix, M. *Atlas of Electrochemical Equilibria in Aqueous Solutions*. National Association of Corrosion Engineers: Houston, TX, 1974.
(25) Hu, S.; Lewis, N. S.; Ager, J. W.; Yang, J.; McKone, J. R.; Strandwitz, N. C. Thin-Film Materials for the Protection of Semiconducting Photoelectrodes in Solar-Fuel Generators. *J. Phys. Chem. C* **2015**, *119* (43), 24201−24228.
(26) Lichterman, M. F.; Sun, K.; Hu, S.; Zhou, X.; McDowell, M. T.; Shaner, M. R.; Richter, M. H.; Crumlin, E. J.; Carim, A. I.; Saadi, F. H.; Brunschwig, B. S.; Lewis, N. S. Protection of inorganic semiconductors for sustained, efficient photoelectrochemical water oxidation. *Catal. Today* **2016**, *262*, 11−23.
(27) Zachaus, C.; Abdi, F. F.; Peter, L. M.; van de Krol, R. Photocurrent of $BiVO_4$ is limited by surface recombination, not surface catalysis. *Chem. Sci.* **2017**, *8*, 3712−3719.
(28) Guevarra, D.; Shinde, A.; Suram, S. K.; Sharp, I. D.; Toma, F. M.; Haber, J. A.; Gregoire, J. M. Development of solar fuels photoanodes through combinatorial integration of Ni-La-Co-Ce oxide catalysts on $BiVO_4$. *Energy Environ. Sci.* **2016**, *9*, 565−580.
(29) Meyer, R.; Sliozberg, K.; Khare, C.; Schuhmann, W.; Ludwig, A. High-Throughput Screening of Thin-Film Semiconductor Material Libraries II: Characterization of Fe-W-O Libraries. *ChemSusChem* **2015**, *8* (7), 1279−1285.
(30) Woodhouse, M.; Parkinson, B. A. Combinatorial approaches for the identification and optimization of oxide semiconductors for efficient solar photoelectrolysis. *Chem. Soc. Rev.* **2009**, *38* (1), 197−210.
(31) Baeck, S. H.; Jaramillo, T. F.; Brandli, C.; McFarland, E. W. Combinatorial electrochemical synthesis and characterization of tungsten-based mixed-metal oxides. *J. Comb. Chem.* **2002**, *4* (6), 563−568.
(32) Gutkowski, R.; Khare, C.; Conzuelo, F.; Kayran, Y. U.; Ludwig, A.; Schuhmann, W. Unraveling compositional effects on the light-induced oxygen evolution in $Bi(V\text{-}Mo\text{-}X)O_4$ material libraries. *Energy Environ. Sci.* **2017**, *10*, 1213−1221.
(33) Jiang, C.; Wang, R.; Parkinson, B. A. Combinatorial approach to improve photoelectrodes based on $BiVO_4$. *ACS Comb. Sci.* **2013**, *15* (12), 639−45.
(34) Jang, J. S.; Lee, J.; Ye, H.; Fan, F. R. F.; Bard, A. J. Rapid Screening of Effective Dopants for Fe_2O_3 Photocatalysts with Scanning Electrochemical Microscopy and Investigation of Their Photoelectrochemical Properties. *J. Phys. Chem. C* **2009**, *113* (16), 6719−6724.
(35) Muñoz, A.; Alonso, J. A.; Casais, M. T.; Martínez-Lope, M. J.; Martínez, J. L.; Fernández-Díaz, M. T. Magnetic structure and properties of $BiMn_2O_5$ oxide: A neutron diffraction study. *Phys. Rev. B: Condens. Matter Mater. Phys.* **2002**, *65* (14), No. 144423.
(36) Zhang, J.; Xu, B.; Li, X. F.; Yao, K. L.; Liu, Z. L. Origin of the multiferroicity in $BiMn_2O_5$ from first-principles calculations. *J. Magn. Magn. Mater.* **2011**, *323* (12), 1599−1605.
(37) Li, N.; Yao, K.; Gao, G.; Sun, Z.; Li, L. Charge, orbital and spin ordering in multiferroic $BiMn_2O_5$: density functional theory calculations. *Phys. Chem. Chem. Phys.* **2011**, *13* (20), 9418−9424.
(38) Volkova, L. M.; Marinin, D. V. Crystal chemistry aspects of the magnetically induced ferroelectricity in $TbMn_2O_5$ and $BiMn_2O_5$. *J. Phys.: Condens. Matter* **2009**, *21* (1), No. 015903.
(39) García-Flores, A. F.; Granado, E.; Martinho, H.; Urbano, R. R.; Rettori, C.; Golovenchits, E. I.; Sanina, V. A.; Oseroff, S. B.; Park, S.; Cheong, S. W. Anomalous phonon shifts in the paramagnetic phase of multiferroic RMn_2O_5 (R = Bi, Eu, Dy): Possible manifestations of unconventional magnetic correlations. *Phys. Rev. B: Condens. Matter Mater. Phys.* **2006**, *73* (10), No. 104411.
(40) Gregoire, J. M.; Van Campen, D. G.; Miller, C. E.; Jones, R.; Suram, S. K.; Mehta, A. High Throughput Synchrotron X-ray Diffraction for Combinatorial Phase Mapping. *J. Synchrotron Radiat.* **2014**, *21* (6), 1262−1268.
(41) Mannsfeld, S. C.; Tang, M. L.; Bao, Z. Thin film structure of triisopropylsilylethynyl-functionalized pentacene and tetraceno[2,3-

DOI: 10.1021/acs.chemmater.7b03591
Chem. Mater. 2017, 29, 10027−10036

b]thiophene from grazing incidence X-ray diffraction. *Adv. Mater.* **2011**, *23* (1), 127−31.
(42) Persson, K. A.; Waldwick, B.; Lazic, P.; Ceder, G. Prediction of solid-aqueous equilibria: Scheme to combine first-principles calculations of solids with experimental aqueous states. *Phys. Rev. B: Condens. Matter Mater. Phys.* **2012**, *85* (23), No. 235438.
(43) Heyd, J.; Scuseria, G. E.; Ernzerhof, M. Hybrid functionals based on a screened Coulomb potential. *J. Chem. Phys.* **2006**, *124* (21), No. 219906.
(44) Perdew, J. P.; Burke, K.; Ernzerhof, M. Generalized gradient approximation made simple. *Phys. Rev. Lett.* **1996**, *77* (18), 3865−3868.
(45) Heyd, J.; Peralta, J. E.; Scuseria, G. E.; Martin, R. L. Energy band gaps and lattice parameters evaluated with the Heyd-Scuseria-Ernzerhof screened hybrid functional. *J. Chem. Phys.* **2005**, *123* (17), No. 174101.
(46) Monkhorst, H. J.; Pack, J. D. Special points for Brillouin-zone integrations. *Phys. Rev. B* **1976**, *13* (12), 5188−5192.
(47) Kresse, G.; Joubert, D. From ultrasoft pseudopotentials to the projector augmented-wave method. *Phys. Rev. B: Condens. Matter Mater. Phys.* **1999**, *59*, 1758−1758.
(48) King-Smith, R. D.; Vanderbilt, D. Theory of polarization of crystalline solids. *Phys. Rev. B: Condens. Matter Mater. Phys.* **1993**, *47* (3), 1651−1654.
(49) Anisimov, V. I.; Aryasetiawan, F.; Lichtenstein, A. I. First-principles calculations of the electronic structure and spectra of strongly correlated systems: the LDA + U method. *J. Phys.: Condens. Matter* **1997**, *9* (4), 767.
(50) Vaugier, L.; Jiang, H.; Biermann, S. Hubbard U and Hund exchange J in transition metal oxides: Screening versus localization trends from constrained random phase approximation. *Phys. Rev. B: Condens. Matter Mater. Phys.* **2012**, *86* (16), No. 165105.
(51) Moses, P. G.; Miao, M. S.; Yan, Q. M.; Van de Walle, C. G. Hybrid functional investigations of band gaps and band alignments for AlN, GaN, InN, and InGaN. *J. Chem. Phys.* **2011**, *134* (8), No. 084703.
(52) Stevanovic, V.; Lany, S.; Ginley, D. S.; Tumas, W.; Zunger, A. Assessing capability of semiconductors to split water using ionization potentials and electron affinities only. *Phys. Chem. Chem. Phys.* **2014**, *16* (8), 3706−3714.
(53) Newhouse, P. F.; Boyd, D. A.; Shinde, A.; Guevarra, D.; Zhou, L.; Soedarmadji, E.; Li, G.; Neaton, J. B.; Gregoire, J. M. Solar fuel photoanodes prepared by inkjet printing of copper vanadates. *J. Mater. Chem. A* **2016**, *4* (19), 7483−7494.
(54) Xiang, C.; Haber, J.; Marcin, M.; Mitrovic, S.; Jin, J.; Gregoire, J. M. Mapping Quantum Yield for (Fe−Zn−Sn−Ti)Ox Photoabsorbers Using a High Throughput Photoelectrochemical Screening System. *ACS Comb. Sci.* **2014**, *16* (3), 120−127.
(55) Zhong, D. K.; Choi, S.; Gamelin, D. R. Near-Complete Suppression of Surface Recombination in Solar Photoelectrolysis by "Co-Pi" Catalyst-Modified W:$BiVO_4$. *J. Am. Chem. Soc.* **2011**, *133* (45), 18370−18377.
(56) Luo, Y.; Tan, G.; Dong, G.; Zhang, L.; Huang, J.; Yang, W.; Zhao, C.; Ren, H. Structural transformation of Sm^{3+} doped $BiVO_4$ with high photocatalytic activity under simulated sun-light. *Appl. Surf. Sci.* **2015**, *324* (Suppl C), 505−511.
(57) Wood, D.; Tauc, J. Weak Absorption Tails in Amorphous Semiconductors. *Phys. Rev. B* **1972**, *5*, 3144−3151.
(58) Biesinger, M. C.; Payne, B. P.; Grosvenor, A. P.; Lau, L. W. M.; Gerson, A. R.; Smart, R. S. C. Resolving surface chemical states in XPS analysis of first row transition metals, oxides and hydroxides: Cr, Mn, Fe, Co and Ni. *Appl. Surf. Sci.* **2011**, *257* (7), 2717−2730.
(59) Ivanova, A. S.; Slavinskaya, E. M.; Mokrinskii, V. V.; Polukhina, I. A.; Tsybulya, S. V.; Prosvirin, I. P.; Bukhtiyarov, V. I.; Rogov, V. A.; Zaikovskii, V. I.; Noskov, A. S. The role of support in formation of the manganese−bismuth oxide catalyst for synthesis of nitrous oxide through oxidation of ammonia with oxygen. *J. Catal.* **2004**, *221* (1), 213−224.
(60) Zhou, L.; Yan, Q.; Yu, J.; Jones, R. J. R.; Becerra-Stasiewicz, N.; Suram, S. K.; Shinde, A.; Guevarra, D.; Neaton, J. B.; Persson, K. A.; Gregoire, J. M. Stability and Self-passivation of Copper Vanadate Photoanodes under Chemical, Electrochemical, and Photoelectrochemical Operation. *Phys. Chem. Chem. Phys.* **2016**, *18*, 9349−9352.
(61) Kresse, G.; Furthmuller, J. Efficient iterative schemes for ab initio total-energy calculations using a plane-wave basis set. *Phys. Rev. B: Condens. Matter Mater. Phys.* **1996**, *54*, 11169−11169.
(62) Onida, G.; Reining, L.; Rubio, A. Electronic excitations: density-functional versus many-body Green's-function approaches. *Rev. Mod. Phys.* **2002**, *74* (2), 601−659.
(63) Giovannetti, G.; van den Brink, J. Electronic Correlations Decimate the Ferroelectric Polarization of Multiferroic $HoMn_2O_5$. *Phys. Rev. Lett.* **2008**, *100* (22), No. 227603.
(64) Chang, T.-R.; Jeng, H.-T.; Ren, C.-Y.; Hsue, C.-S. Charge-orbital ordering and ferroelectric polarization in multiferroic $TbMn_2O_5$ from first principles. *Phys. Rev. B: Condens. Matter Mater. Phys.* **2011**, *84* (2), No. 024421.
(65) Niizeki, N.; Wachi, M. The crystal structures of $Bi_2Mn_4O_{10}$, $Bi_2Al_4O_9$, and $Bi_2Fe_4O_9$. *Z. Kristallogr. - Cryst. Mater.* **1968**, *127*, 173.
(66) Kim, J. W.; Haam, S. Y.; Oh, Y. S.; Park, S.; Cheong, S. W.; Sharma, P. A.; Jaime, M.; Harrison, N.; Han, J. H.; Jeon, G.-S.; Coleman, P.; Kim, K. H. Observation of a multiferroic critical end point. *Proc. Natl. Acad. Sci. U. S. A.* **2009**, *106* (37), 15573−15576.
(67) Walsh, A.; Yan, Y.; Huda, M. N.; Al-Jassim, M. M.; Wei, S. H. Band Edge Electronic Structure of $BiVO_4$: Elucidating the Role of the Bi s and V d Orbitals. *Chem. Mater.* **2009**, *21*, 547−551.
(68) Cooper, J. K.; Gul, S.; Toma, F. M.; Chen, L.; Glans, P.-A.; Guo, J.; Ager, J. W.; Yano, J.; Sharp, I. D. Electronic Structure of Monoclinic $BiVO_4$. *Chem. Mater.* **2014**, *26* (18), 5365−5373.
(69) Abdi, F. F.; Chemseddine, A.; Berglund, S. P.; van de Krol, R. Assessing the Suitability of Iron Tungstate (Fe_2WO_6) as a Photoelectrode Material for Water Oxidation. *J. Phys. Chem. C* **2017**, *121* (1), 153−160.
(70) Jiang, C.-M.; Farmand, M.; Wu, C. H.; Liu, Y.-S.; Guo, J.; Drisdell, W. S.; Cooper, J. K.; Sharp, I. D. Electronic Structure, Optoelectronic Properties, and Photoelectrochemical Characteristics of γ-$Cu_3V_2O_8$ Thin Films. *Chem. Mater.* **2017**, *29* (7), 3334−3345.

DOI: 10.1021/acs.chemmater.7b03591
Chem. Mater. 2017, 29, 10027−10036